REVIEW ARTICLE

Quantum simulation of molecular interaction and dynamics at surfaces

Zi-jing DING (丁子敬), **Yang JIAO** (焦扬), **Sheng MENG** (孟胜)†

Beijing National Laboratory for Condensed Matter Physics, and Institute of Physics, Chinese Academy of Sciences,
Beijing 100190, China

E-mail: †smeng@iphy.ac.cn

The interaction between molecules and solid surfaces plays important roles in various applications, including catalysis, sensors, nanoelectronics, and solar cells. Surprisingly, a full understanding of molecule–surface interaction at the quantum mechanical level has not been achieved even for very simple molecules, such as water. In this mini-review, we report recent progresses and current status of studies on interaction between representative molecules and surfaces. Taking water/metal, DNA bases/carbon nanotube, and organic dye molecule/oxide as examples, we focus on the understanding on the microstructure, electronic property, and electron–ion dynamics involved in these systems obtained from first-principles quantum mechanical calculations. We find that a quantum mechanical description of molecule–surface interaction is essential for understanding interface phenomenon at the microscopic level, such as wetting. New theoretical developments, including van der Waals density functional and quantum nuclei treatment, improve further our understanding of surface interactions.

Keywords adsorption, quantum simulation, density functional theory, electronic structure, electron dynamics

PACS numbers 68.43.Bc, 68.35.Ja, 73.63.-b, 82.30.Rs

Contents

1 Introduction

The interaction of molecules, including organic and biologically important ones, with solid-state surfaces and nanostructures plays a central role in many important applications, such as molecular electronics, solar cells, and biosensors. For instance, organic solar cells are built upon organic molecules and their interfaces with solid electrodes (such as oxides or metals), and have attracted rapidly growing attentions due to the potential application in the low-cost, environmental friendly, flexible, and large-scale photovoltaic devices [1, 2]. Much research has been focused on understanding the microstructure at the molecular level, the mechanism of electronic interaction, and the ion and electron dynamics of the molecule–surface interface. To understand surface interactions and dynamics, theory plays an indispensable role because most experimental tools are not surface sensitive and performing experiments at nanoscale is extremely challenging. Among various theoretical approaches, simulations based on quantum mechanical treatments are most promising thanks to their high accuracy, univer-

sal of molecule–surface interaction. In this article, we review recent progresses made on the quantum simulations of molecule–surface interaction. Three representative examples were chosen: i) water on metal surfaces, ii) DNA nucleosides on carbon nanotubes (CNTs), and iii) organic dye molecules on TiO_2.

2 Quantum mechanical simulations

Quantum mechanical methods describe intra- and intermolecular bonds, structural characteristics, and dynamical behaviors of molecules on surfaces by solving electronic Schrödinger's equation at the atomic level. They predict changes in bond lengths, bond angles, and electrostatic polarization with respect to environmental stimuli, which are hard to describe in classical simulations if not impossible. Furthermore, since no system-specific empirical parameters are used, ab initio methods could produce a universal high accuracy and overcome ambiguities in classical models. These advantages will help us to obtain a unified picture of molecules in different environments, for instance, on various surfaces, and produce reliable parameters for classical simulations. This is more pronounced at the nanometer scale — in fact, it is effectively the only reliable approach to predict molecular behaviors at the few-molecule level. At this level, empirical parameters, fitted to reproduce bulk properties of molecules, always fail [3]. Ab initio methods have been successfully applied to study molecular interactions and dynamics on surfaces [4–10]. Together with experimental information obtained by surface science tools, such as scanning tunnelling microscopy (STM), quantum mechanical simulations have revealed the atomic, electronic, and optical properties of surface-based molecular structures and associated ion and electron dynamics for diffusion, dissociation, vibration, and photoexcition [10–14].

On the other hand, the computational cost of quantum mechanical calculations and simulations is often very large: usually the system size (hundreds of atoms, or a few thousands of electrons) and the timescale (a few femtoseconds to tens of picoseconds) they could deal with are one to three orders of magnitude smaller than those from classical simulations. Developing schemes with better scalability is a way to overcome this difficulty [15]. In addition, although the accuracy in quantum simulations at about 1 kcal/mol∼40 meV, is much improved than that from empirical calculations, they are less reliable in the cases where weak interactions are dominant, such as van der Waals (vdW) forces in biological environments. Different choices of exchange-correlation functionals in density functional calculations are another source of discrepancy. All these facts imply a limitation of the current quantum mechanical approaches and point to directions for future developments.

Most of the quantum mechanical simulations described in this work are based on first-principles calculations within the framework of Density Functional Theory (DFT) [16, 17]. Calculations were performed using Vienna *ab initio* simulation package (VASP) [18] and SIESTA code [15]. We model the surface by a super-cell slab geometry. For the calculations using VASP, we use projector-augmented-wave pseudopotentials [19] to model the atomic cores and the PBE form of generalized gradient approximation (GGA) [20] to describe exchange-correlation (XC) energies, which are the most reliable in describing the hydrogen bonds (H-bonds) and properties of water [21], as well as surface properties [22]. In SIESTA, we use pseudopotentials of the Troullier–Martins type [23], the Ceperley–Alder form of the local density approximation (LDA) [24] and PBE functional, and a local basis set of double-ζ polarized orbitals (13 orbitals for C, N, F, and O and 5 orbitals for H). Since van der Waals forces are important for such weakly interacting systems, we also use vdW-density functionals (vdW-DF) of the Lundqvist–Langreth type [25] to study binding configurations and energies. An auxiliary real-space grid equivalent to a plane-wave cutoff of 120 Ry is employed.

For geometry optimization, a structure is considered fully relaxed when the magnitude of forces on the atoms is smaller than 0.04 eV/Å. Ab initio molecular dynamics (MD) simulations use forces calculated from DFT and proceed the Newtonian ionic trajectory at a target temperature in the constant-energy mode. Optical absorbance is calculated within the linear response regime [26] of time-dependent DFT (TDDFT) [27] by propagating electronic wavefunctions 6107 steps in time after abruptly turning off a perturbing external field of 0.1 V/Å. The timestep of simulations is 0.0034 fs, corresponding to an energy resolution of 0.1 eV.

In order to simulate interface electron dynamics, the non-adiabatic evolution of both electrons and ions in real time is monitored after excitation. The time-dependent Kohn–Sham equations of electrons and the Newtonian motion of ions are solved simultaneously, with ionic forces along the classical trajectory evaluated through the Ehrenfest theorem [28]. The electron density is updated self-consistently during the real-time propagation of single-particle Kohn–Sham wavefunctions with a timestep of 0.02419 fs. The initial velocity of ions is assigned according to the equilibrium Boltzmann–Maxwell distribution at a given temperature.

3 Water adsorption on metal surfaces

We start from a simple model system: water on metals. Water adsorption on metal surfaces [29, 30] has

received intensive investigations since 1970s due to its key roles in catalysis and wetting as well as the explosive development of modern surface analysis techniques, such as low-energy electron diffraction (LEED), high-resolution electron energy loss spectroscopy (HREELS), and STM. This section gives a brief summary on the microscopic structure of water on metal surfaces and recent molecular-level understanding achieved from quantum mechanical simulations.

3.1 Two-dimensional water overlayers

In 1980s, water adsorbed on closely packed precious metal surfaces Ru(0001), Pt(111), and Rh(111) was characterized to have a $(\sqrt{3} \times \sqrt{3})R30°$ pattern using LEED [29]. Since the lattice constant of these hexagonal surfaces is very close to that of bulk ice Ih (0001) surface ($4.51\text{Å} \times 4.51\text{Å}$), it was widely believed that water forms bilayers on metal surfaces: a water molecule is connected to three neighboring water molecules by H-bonds, constituting a puckered hexagonal network, see Fig.1. However, such an idea was soon challenged by both experiment and theory. In 1994, Held *et al.* first found that the so-called water bilayer on Ru(0001) is actually a planar "single-layer" with a thickness $\leqslant 0.1$ Å in LEED analysis [31]. Based on this result, Feibelman proposed a half-dissociated overlayer model in 2002 [9]. In this model, a half of water molecules are partially dissociated, leaving their OH and H groups adsorbed on top of Ru atoms and forming H-bonds with neighboring nondissociated water molecules. The model yields a geometry very close to that from LEED analysis; moreover, quantum mechanical calculations based on DFT predict that this half-dissociated structure is ~ 0.2 eV/H$_2$O more stable than the intact bilayers.
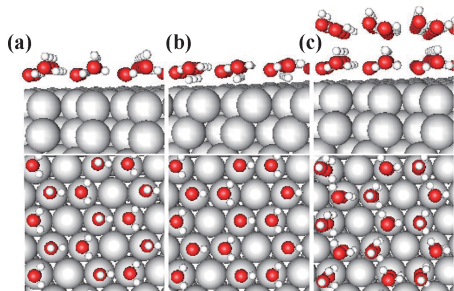
Fig. 1 Atomic structure of **(a)** H-up and **(b)** H-down bilayer on a closely packed metal surface, and **(c)** a two-bilayer structure.

Whether the half-dissociated layer truly exists on Ru(0001) invoked intense discussion and much controversy in the following years. For instance, the experimental infrared absorption spectrum is closer to calculated ones for the intact bilayer rather than for the half-dissociated layer [32]. It questioned if the half-dissociated model is the real structure observed in experiment.

Through the following years of research and discussion, a consensus concerning whether water dissociates on Ru(0001) was finally reached: half-dissociated water layers do exist but have to be activated (by high-energy electrons, heat, etc.) [6]. This resolves the inconsistency in different experiments and contradictions between theory and experiment. However, the molecular structure for the intact wetting layer on Ru(0001) is still unknown.

Despite the similar geometry among closely packed metal surfaces, it turns out that the half-dissociated layer is not a general structure. Shortly after Feibelman's proposal, Meng *et al.* showed that, on Pt(111), intact bilayers are more stable than the half-dissociated layer by > 0.24 eV/H$_2$O [4]. Through ab initio MD simulations, they also obtained vibrational spectra for various water structures on Pt(111): vibrational frequencies agree well with measured values in HREELS experiment [33] if an intact layer were assumed. In addition, the authors identified that there are two kinds of H-bonds with different strengths in a water bilayer: a strong H-bond and two weak H-bonds per $(\sqrt{3} \times \sqrt{3})R30°$ unit cell due to the asymmetry in OH coordination. Ogasawara *et al.* performed X-ray absorption experiments and reached a similar conclusion, namely, water does not dissociate on Pt(111) [34]. Intact wetting layers on Pt(111) were identified to have a complex periodicity [35, 36], $(\sqrt{37} \times \sqrt{37})R25.3°$ for incomplete layers and $(\sqrt{39} \times \sqrt{39})R16.1°$ for complete layers in helium atom scattering [37] and LEED experiments [38], and most recently in STM [39].

Water adsorption on Cu(110) surface is another interesting case. Whether the $c(2\times2)$ and (7×8) water phases observed experimentally [40] contain dissociative water molecules attracts many discussions, with controversial evidences for each case. According to Ren *et al.*'s calculation, the two structures are very close in energy [7, 8]. It indicates that Cu(110) surface is a borderline for dissociative and intact water adsorption. The authors carried out ab initio MD simulations for both intact and dissociated water layers. The vibrational spectrum is extracted from MD trajectory, and compared with experimental result in Fig. 2. The intact layer was found to be consistent with experimental spectrum and new measurements performed after the paper was published [40]. This study further confirmed that water initially adsorbs molecularly on Cu(110); however, water dissociation could be activated by high energy electron- or photon-beam illumination during measurements. The detailed atomic structure in (7×8) phase before dissociation, however, is still a challenge to the surface science community.

3.2 One-dimensional water chains

Besides two-dimensional monolayers and multilayers, water also forms interesting structures of other dimen-
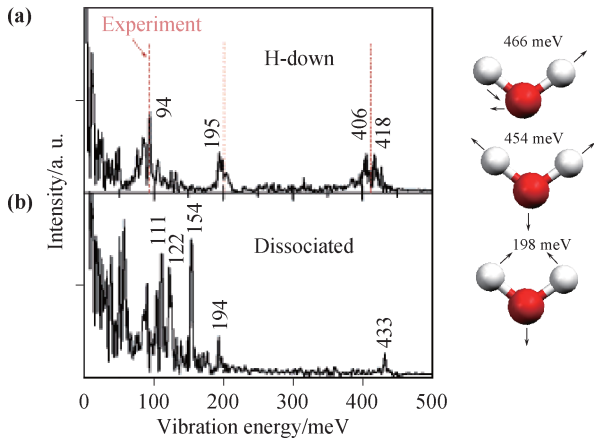
Fig. 2 Calculated vibrational spectrum from ab initio MD simulations for **(a)** intact H-down bilayer and **(b)** half-dissociated overlayer on Cu(110). Experimental vibration frequencies are also indicated (vertical dashed lines). Right panels show schematically vibrational modes and energies for an isolated water molecule.

sions. For instance, under certain conditions water forms one-dimensional chains. Some examples include:

(1) As early as in 1995, Held *et al.* observed that H_2O forms stripes with a width of 6.5 substrate lattice constants on Ru(0001) [41]. They have a general one-dimensional character and present an isotopic effect.

(2) On the steps of Pt(111) surface, water prefers to adsorb at the upper side of the step as a one-dimensional chain with a width close to single water molecule [42]. Through ab initio calculations, Meng *et al.* proposed that the water chain is a zigzag structure with one OH of each water connects the neighboring molecules and the other OH bond points inward or outward of the step alternately [5]. They also showed that the structure on steps is indeed energetically more favorable than on terraces.

(3) In 2006, Yamada *et al.* observed one-dimensional water chains on Cu(110) along the [001] direction [43]. In addition, these chains are well separated and parallel to each other, indicating a repulsive interaction between them. Carrasco *et al.* identified the molecular structure of these parallel water chains by comparing their high-resolution STM images with those from quantum simulations [10]. Surprisingly, they found that the water chains are built up from an arrangement of water pentagons instead of hexagons! The latter is believed for long to be the only stable constituent for ice structures. The presence of ice pentagons on Cu(110) is a result of strong surface confinement, namely the large strain in water hexagons pinned on Cu(110) substrate is released by forming looser water pentagons while optimized water-Cu interactions are maintained. In fact, ice overlayers composed by tetragonal and octagonal H-bond network have been already proposed to explain water adsorption behavior on SiO_2 [44] and salt [45].

(4) Other one-dimensional water chains also exist on Cu(110) surface, forming (2×1) reconstructions along

[110] [46]. It is generally considered as a result of large amount of OH groups involved in the structure.

3.3 Water clusters

At low coverage, water molecules arrange themselves to form finite structures, see Fig. 3. Water monomer is believed to exist only at extreme low temperatures (<20 K), since water diffuses easily on metal surfaces and forms clusters. The rapid diffusion was directly observed by Mitsui *et al.* in 2002 using STM [47]. A peculiar observation is that water dimer diffuses 10^4 times faster than monomer on Pd(111) at low temperature (40 K). Meng *et al.* revealed in 2002 the adsorption structures of both water monomer and dimer on a metal surface: both adsorb on top site of metal atoms [4]. One of the two molecules in a water dimer is closer to the surface than the other, with its oxygen atom directly bonded to the metal atom. The lower water molecule donates a strong H-bond to the upper one, which only interacts weakly with the metal surface through its two low-lying H atoms (Fig. 3). Based on this optimized geometry for a surface water dimer, if one assumes that the diffusion process involves hopping from one top site to another, the dimer and the monomer will experience a similar potential barrier during diffusion (~ 0.15 eV). This would contradict above experimental observation. To resolve this puzzle, Ranea *et al.* proposed that the tunnelling process during water dimer diffusion is the key [48]. The diffusion of a dimer proceeds via three consecutive steps: i) upper water rotation around the fixed lower water, ii) upper-lower water exchange, and iii) rotation of the new upper molecule. The first and last steps proceed with little barrier, while the height exchange of the two molecules is dominated by the quantum tunneling of four hydrogens through a barrier ~ 0.22 eV. At low temperatures (<70 K), this tunnelling process is much faster than thermal activated over-barrier processes, resulting in the faster diffusion of water dimer than a mononer.
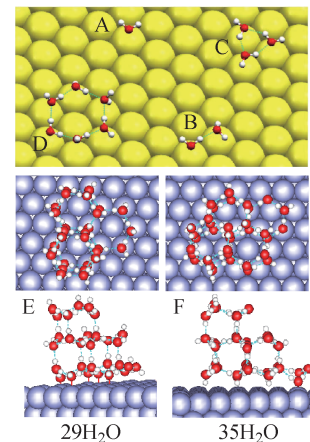
Fig. 3 Small water clusters on a metal surface: (A) Monomer, (B) dimer, (C) trimer, (D) hexamer, (E) $(H_2O)_{29}$, and (F) $(H_2O)_{35}$.

An interesting cluster is water hexamer, which is said to be the smallest ice block [49]. Water hexamers have been observed on Ag(111) [50] and Cu(111) surfaces [51]. The effect of different metal surfaces on the thickness of the hexamer and hydrogen bond lengths has been analyzed [51]. Meng *et al.* investigated adsorption of small water clusters up to a size of $(H_2O)_{35}$, the latter could serve as a model for three-dimensional water clusters on surface [52].

3.4   General trends from quantum simulations

With above data from both experimental and theoretical investigations, we try to summarize some general features and trends for water adsorption on different metal surfaces, especially the trends for water monomers and bilayers adsorption [5].

(1) Regarding the bonding geometry of water/metals, it is generally observed that water prefers to lie flatly near the top site of metal surfaces whenever possible, to optimize water–metal interaction. The adsorption height of monomers and the bottom water in bilayers increases gradually in the order of Ru<Rh<Pd<Pt<Au, while the height of the upper water keeps at 3.40 Å for H-up and 3.20 Å for H-down bilayer, as shown in Fig. 4. The structure also varies with water coverage. It is found that on Pt(111) the adsorption height of the bottom water shrinks from 2.69 to 2.63, 2.56, 2.49, 2.52, and 2.47 Å, respectively, when the overlayer grows from 1 to 6 bilayers. In contrast, the height of the up water in the first bilayer remains constant, 3.25±0.02 Å [Fig. 4(b)]. The constant height of the up water molecule in the first bilayer indicates that the water–surface interaction is localized dominantly in the bottom layer and seems to be a universal result for water adsorption on metal surfaces.
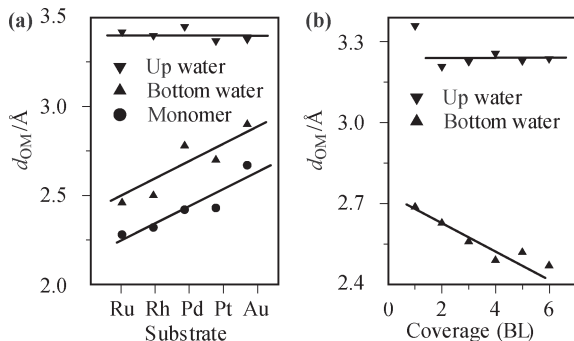
Fig. 4 The distance between O in water and the metal atom beneath it, d_{OM}, as a function of **(a)** the substrate, and **(b)** the water coverage. In (a) the d_{OM} for water monomers, and for the bottom water and up water in the H-up bilayers on different surfaces are shown. In (b) d_{OM} for the bottom and up water in the first bilayer upon 1–6 bilayers adsorption on Pt are plotted. Lines are for guidance to the eye.

(2) On the strength of water–surface bond, the adsorption energy of water monomers follows the same order Ru>Rh>Pd>Pt>Au, as in the periodic table. This in-

dicates the close correlation between d-band occupancy and water–metal bonding. Water–metal bond involves mainly d-band–lone pairs interaction, the more unoccupied d states above the Fermi level, the stronger water–surface bonding is. Meanwhile, the adsorption energy of bilayers on these metals makes little difference between each other, except on Au, because of the modulation in H-bonds.

(3) We are also concerned about how much the surface affects water, the H-bonding, and its dynamics. The answer can vary from case to case. The OH bond of water is elongated and HOH angle is widened upon adsorption. This indicates some charge transfer from O in water to metal surfaces. Detailed analysis suggests that the amount of charge transfer is on the level of $0.02e$ per molecule. H-bonds are generally enhanced upon adsorption. The H-bond lengths are usually shortened on surfaces. In the dynamics aspect, the diffusion barrier is found to vary from surface to surface, ranging from 0.1 (Au) to 0.3 eV (Ru) due to the different binding strengths of water. The surface is also found to influence the proton transfer process significantly [36].

On the other hand, water does not influence much the structure of the surface. The relaxation of the surface layer is usually minor, on the level of ⩽0.05 Å. The metal atom beneath the adsorbed water is usually pulled out by 0.02–0.04 Å. The anti-correlation effect in the oxygen–metal separations, namely, the metal atom beneath the bottom water molecule is pulled up while the atom beneath the upper H_2O moves further into bulk, is also observed, and in qualitative agreement with experiments [31]. This effect leads to a surface roughness of about 0.1 Å in bilayer adsorption on metal surfaces.

3.5   Quantum motion of H atoms

We note that quantum effects of hydrogen nuclei in water are important. Due to the small mass of hydrogen, it is interesting to find out how the dynamical properties of water change in the quantum-mechanical treatment of H. The quantum effect of hydrogen nucleus was found to reduce the barrier of proton transfer from 55 to 15 meV during OH^- transport in liquid water, and therefore promote the proton transfer/tunnelling probability significantly [53]. While for $H_3O_2^-$ clusters in gas phase [54] and hydrated H_3O^+ in liquid water [55], this barrier is completely washed out by nuclear quantum effects. It also plays a role in water diffusion. The rearrangement of H-bonds through quantum tunnelling is essential to the rapid diffusion of water dimers on Pd(111) observed in experiment [48]. As a prototype system, we have treated the H-up and H-down bilayer conversion and bilayer dissociation explicitly in both classical nudged elastic band (NEB) method and the quantum terrain. We find that the small barrier between the H-up and H-down bilayer

is further lowered by quantum rotation of the upper H_2O molecule, and the tunnelling motion is dominant at temperatures below 115 K.

We model the system by a one-dimensional double-well potential and then solve the Schrödinger equation for H_2O numerically. First, we recalculate the barrier by including the zero-point energy of H motion. In Fig. 5, a double-well potential and the eigen wavefunctions for the H-up/H-down bilayer conversion on Pt(111) are sketched. The potential is calculated from first-principles by NEB method and then fitted by a quartic function. The potential well A and B, separated in energy by $E_A - E_B \simeq 24$ meV, represent the H-up and H-down bilayers, respectively. Between them is a classical migration barrier with a height as small as $E_c = E_C - E_A \simeq 76$ meV. Assuming the heavy atoms are frozen during the quantum rotation of the water molecule, solution of the Schrödinger equation for H_2O rotation in this potential identifies the lowest bound state at an energy of $E_{A0} = 33$ meV, which is predominant in potential well A. The other bound state, which has the lowest bound energy but still higher than the classical barrier E_c, is located at $E_{A1} = 90$ meV with the wavefunction extended throughout the whole double-well (Fig. 5). Thus, by including the quantum rotation in water, the quantum barrier for H-up/down conversion is found to be $E_q = E_{A1} - E_{A0} = 90 - 33 = 57$ meV, lowered by 19 meV compared to the classic barrier. Using a D_2O molecule, the quantum barrier increases by 4 meV.
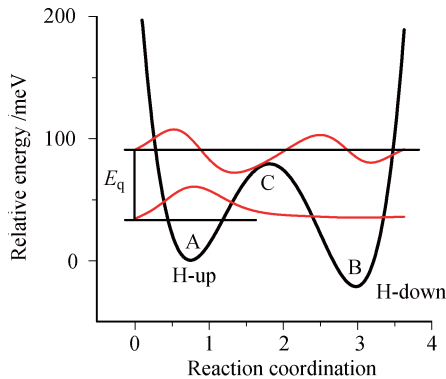
Fig. 5 The fitted potential for H-up/H-down bilayer conversion on Pt(111). The two eigenvalues and corresponding wavefunctions for H_2O rotation are also shown.

At low temperatures, proton tunnelling through the barrier is important or even dominant. The WKB approximation for the tunnelling probability is

$$\Gamma = e^{\frac{-2}{\hbar} \int \sqrt{2m[V(x)-E]}dx} \simeq e^{-\alpha\sqrt{E_q}} \qquad (1)$$

where α takes a value of 24 eV$^{-1/2}$, corresponding to the mass of 2 H and potential minima separated by 1.4 Å. The quantum tunnelling rate and the rate for overcoming the barrier is then

$$D_q = We^{-\alpha\sqrt{E_q}} \quad \text{for quantum tunnelling}$$
$$D_c = We^{-E_q/(k_BT)} \quad \text{for classical activation} \qquad (2)$$

respectively, where W is the attempt frequency, $W = \frac{k_BT}{h}[e^{\hbar\omega/(k_BT)} - 1]$. With realistic parameters, the rate of quantum tunnelling is dominant in H-up/H-down conversion below a temperature of about 115 K, where $D_q > D_c$. At this temperature, the tunnelling rate is determined to be 2×10^{11} s^{-1}.

Employing the same approach, the barrier for bilayer dissociation on Ru(0001) is found to be lowered by 30 meV (D_2O) and 100 meV (H_2O), respectively, when including the quantum motion of the intermediate H atom, while the classical barrier is 0.62 eV, calculated from NEB method. The different barriers for H_2O and D_2O dissociation, compared to the desorption barrier of 0.53 eV (above or below), which is hardly affected by quantum motion of water, explain why some fraction of H_2O is dissociated while no D_2O dissociation occurs in experiments at low temperatures [32, 56, 57].

The quantum nuclear effect in surface water adlayers has also been studied recently using an ab initio path integral approach. Li *et al.* have looked at the quantum delocalization of H atoms in a mixed water and hydroxyl layer [58]. Interestingly, they found that, on strongly bonded Ni(111) surface, the conventional distinction between a covalent OH bond and a H-bond disappears completely due to sharing of H by two oxygen atoms whose distance is strongly strained by the presence of substrate.

3.6 van der Waals density functional investigation

In conventional density functionals, such as LDA or GGA, the long-range vdW interaction is not included, which could produce an underestimated adsorption energy for water layers on surfaces. During the last decades, there have been persistent efforts to build vdW interactions into density functional and great progress has been achieved only recently. Lundqvist, Langreth, and collaborators proposed a nonlocal correlation function that could describe long-range vdW energies in molecular and extended systems [25],

$$E_c^{nl} = \frac{1}{2} \int dr dr' n(r)\phi(r,r')n(r') \qquad (3)$$

The new density functional is then,

$$E_{xc}^{vdW} = E_x^{GGA} + E_c^{LDA} + E_c^{nl} \qquad (4)$$

Note that, in the original proposal, the revPBE form of GGA exchange is used for the best match with parameters used in E_c^{nl}. Recently, other choices of GGA exchange have been tested and optimized.

We have applied this approach to investigate the bonding between intact and dissociative water layers on Cu(110). The adsorption energies from different func-

tionals are summarized in Fig. 6. It is clearly seen that, for all XC functionals used here, the H-down layer has the largest absorption energy among the three overlayer structures. The energy differences between H-down and H-up layers are 0.08, 0.06, 0.06, and 0.03 eV in PBE, revPBE, vdW-DF/PBE (the label denotes a vdW density functional with PBE exchange; the same rule follows throughout this paper), and vdW-DF/revPBE, respectively. The inclusion of vdW interactions decreases the energy differences between the two intact structures, largely because, in the H-up layer, the vdW attraction between the upper water and the Cu surface not counted by any means in GGA (even not via OH···Cu bonding as in the H-down layer) is now included. The energy differences between H-down and half-dissociated layers are larger, being 0.11, 0.14, 0.10, and 0.16 eV for PBE, revPBE, vdW-DF/PBE, and vdW-DF/revPBE, respectively. In the current approach using local bases, intact layers have a higher adsorption energy, at variance with the plane-wave results with a sparse k-point sampling [7]. Nevertheless, for all functionals used here, the energy difference between intact and dissociative adsorption does not exceed 0.16 eV per H_2O, indicating that the two structures are close in energy and Cu(110) is a borderline case for intact and dissociative water adsorption [7]. We also notice that the revPBE functional generally produces the binding energies too low to be reasonable for water adsorption, almost at the half value of that from PBE functional. Consequently, vdW-DF employing a revPBE exchange also yields lower energies, as compared to PBE and vdW-DF/PBE.
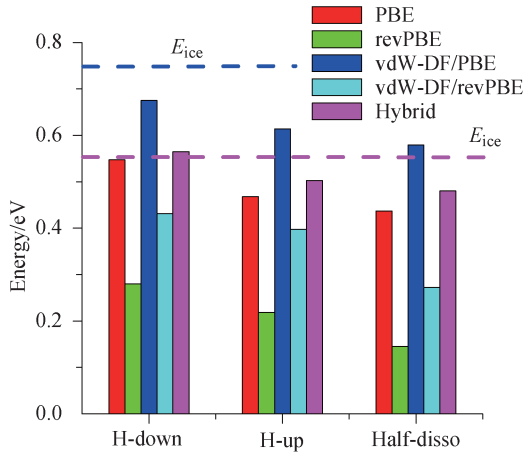
Fig. 6 Adsorption energies of water overlayer on Cu(110) in various density functionals and the hybrid vdW approach. Dashed lines indicate the cohesive energy of ice Ih in vdW-DF/revPBE (*magenta*) and vdW-DF/PBE (*blue*).

More importantly, all the reported energies for water overlayer structures are lower than the corresponding cohesive energy (E_{ice}) of bulk Ice Ih. Employing a 12-molecule Hamann's model for Ice Ih [21], we have calculated the cohesive energy of ice being 0.638 eV in

PBE, 0.741 eV in vdW-DF/PBE, and 0.560 eV in vdW-DF/revPBE. With these numbers it means thermodynamically no water overlayers considered above would wet the Cu(110) surface, at variance with experimental observation [40].

We propose a hybrid vdW-DF approach for obtaining adsorption energies of water structures on metal surfaces, namely, to use vdW-DF/revPBE for describing H-bonds in ice adlayers (since it produces the best result for ice Ih) and vdW-DF/PBE for water–Cu interactions to remedy the underbinding problem in other functionals. In practice, we calculate the adsorption energy of a single water molecule in the same configuration as in the water overlayers using both vdW-DF/PBE and vdW-DF/revPBE, their energy difference ΔE_a is then added into the vdW-DF/revPBE adsorption energy of the corresponding overlayer on surface. In doing this, we assume that the water–Cu interaction is not much disturbed by the presence of H-bonds between water molecules and can be separated from H-bonding interactions. Effectively, this amounts to the vdW-DF/PBE treatment of water–Cu bonds, and vdW-DF/revPBE of H-bonds for water overlayer adsorption on surfaces, as formulated above. It turns out that vdW-DF/revPBE energies of single-water adsorption are quite similar to PBE results, but both are much smaller than vdW-DF/PBE values. The differences between the two vdW-DFs are added to the vdW-DF/revPBE adsorption energy of water overlayers on Cu(110). The numbers (H-down: 0.565 eV; H-up: 0.503 eV; half-dissociated: 0.480 eV) are now much closer to the cohesive energy of ice E_{ice} (0.56 eV within vdW-DF/revPBE). In particular, the H-down layer has a larger adsorption energy than E_{ice}, indicating that it wets the Cu(110) surface thermodynamically, as observed in experimen [40]. The (7×8) structure with the majority of H-down water configuration is observed to be a wetting layer on Cu(110). In reality, a mixture of H-up and H-down layers in a larger periodicity will have a larger adsorption energy, confirming further its wetting ability. In addition, our results seem to suggest that the wetting behavior of half-dissociated layer may have a different origin: the hydrogen atoms from dissociated water molecules will easily diffuse away along [110] grooves forming hydrogen molecules and being desorbed; the mixed OH+H_2O layer that is left has a very large binding energy to Cu(110) (considering free OH and H_2O as references). Consequently, the half-dissociated layer is highly stable and wetting.

3.7 Microscopic picture of water wetting

Water wetting on surfaces is a ubiquitous and important phenomenon. It sensitively affects the mechanical properties (i.e., lubrication), chemical reactivity, hydrophilicity and other functions of surfaces and interfaces. It also

has a direct implication for water in biological systems and biomedical applications. The wettability of surfaces can be rationalized by energetics at the microscopic scale, since, on such a scale, the macroscopic concept of contact angle does not apply. The ratio between H-bond energy and water adsorption energy (for monomers), $\omega = E_{HB}/E_{ads}$, is defined as a quantity characterizing the wettability of a metal surface [49]. Qualitatively, $\omega = 1$ is the rough border between hydrophilic and hydrophobic interactions. The calculated wettability shows an order of ω as $\omega_{Ru} \leqslant \omega_{Rh} < \omega_{Pd} \leqslant \omega_{Pt} < \omega_{Au}$, giving a wetting order of Ru>Rh>Pd>Pt>Au. The Ru, Rh, Pd, and Pt surfaces lie in the hydrophilic region; on the contrary, Au is in the hydrophobic region, in agreement with experimental observations [59, 60]. The wetting order results essentially from the variation of the water–metal interaction on these surfaces, because the H-bond energy does not change appreciably on different surfaces.

3.8 Application: Designing a superhydrophilic surface

Based on the above microscopic criterion for water wetting, we strive to apply it to the design of surfaces with a desired wetting property. As an example, we design a surface with extreme hydrophilicity. Using diamond as a model, Meng *et al.* showed that the naturally hydrophobic behavior of a hydrogen-terminated C(111) surface can be manipulated by replacing the H termination with a monolayer of adsorbates [61]. In particular, a mixed monolayer of $\frac{1}{3}$Na and $\frac{2}{3}$F atoms leads to superhydrophilic behavior, as characterized by an $\omega = 0.5$ in first-principles calculations. The physical origin of the superhydrophilic behavior is attributed to the ionic nature of the Na adatoms, which mediate the *right* degree of binding strength between water molecules and the substrate.

4 DNA bases identification using nanotubes

We now move to a more complex system comprising a representing biological molecule, DNA, and a prototype nanostructure, CNT. Both DNA strands and CNTs are prototypical one-dimensional structures. Single-stranded DNA (ssDNA) and CNTs have complementary structural features: ssDNA is a flexible, amphiphilic biopolymer, while CNTs are stiff, strongly hydrophobic nanorods. Therefore, they can be assembled to form a stable hybrid structure. Indeed, ssDNA of different lengths, either small oligomers consisting of tens of bases [62, 63] or long genomic strands (∼100 bases) [64], wrap around single-wall CNTs forming tight helices, as observed by atomic force microscopy (AFM). Similarly, double-stranded DNA (dsDNA) [65, 66] and fragmented dsDNA (a hybrid of both ssDNA and dsDNA) [67] can

also be associated with a CNT though less efficiently. In addition, as predicted theoretically [68, 69] and confirmed experimentally [70] by high-resolution transmission electron microscopy, DNA can be encapsulated into the CNT interior. While the structures of DNA and CNTs, each in its natural form and environment, are well established (e.g., the B-DNA form in solution [71], or isolated CNTs [72]), the molecular structure for the combined DNA–CNT systems and the nature of the electronic interaction remain elusive [62–65, 73–78]. We have employed a quantum mechanical approach based on DFT to describe the atomic, electronic, and optical properties of DNA–CNT hybrid [11, 12].

4.1 Adsorption structure

The first step in attempting to understand the DNA–CNT interaction is to establish the possible binding geometries in a DNA-CNT system, beginning with the structure of a single nucleotide adsorbed on the CNT surface [11]. In order to study this local interaction, we have used nucleosides, consisting of a base, a deoxyribose sugar group and terminated by OH at the 3' and 5' ends. The phosphate group of a nucleotide is not included (in the following, we identify nucleotides by the same symbols as the bases). We use the semiconducting (10, 0) nanotube, which is abundant during synthesis and has a diameter of 7.9 Å, as a representative CNT. We first determined the energetically favorable configurations of the nucleosides on the nanotube with the CHARMM program [79] using the standard force-fields [80]; the structures were further optimized using DFT in LDA. The structural relaxation was carried to the point that the calculated forces on each atom have a magnitude smaller than 0.005 eV/Å.

Compared to the planar structure of graphene, CNTs have a curved surface that perturbs only slightly the nucleoside adsorption positions but results in many inequivalent adsorption geometries. We performed an extensive search of the potential energy surface of each adsorbed nucleoside with the successive confinement method [81]. The potential energy surfaces of biomolecules are extremely complicated [82–84] and currently preclude direct exploration with ab initio methods. The search returned 1000 distinct potential energy minima for each base/CNT system, with the global energy minimum structures shown in Fig. 7. The room temperature populations of each minimum range from 10^{-10} to 50%. Despite the numerous configurations, we found that only very few of them are dominant with significant room temperature populations. For instance, there are only three dominant configurations for A, with populations of 28.4%, 27.6%, and 10.1%; three configurations for G (populations: 45.9%, 20.8%, and 7.2%), and four for T (populations: 11.2%, 5.0%, 4.1%, and 2.0%), and four

for C (populations: 25.2%, 6.8%, 4.3%, and 3.2%). Together, these three to four structures represent the majority of the total population of configurations.
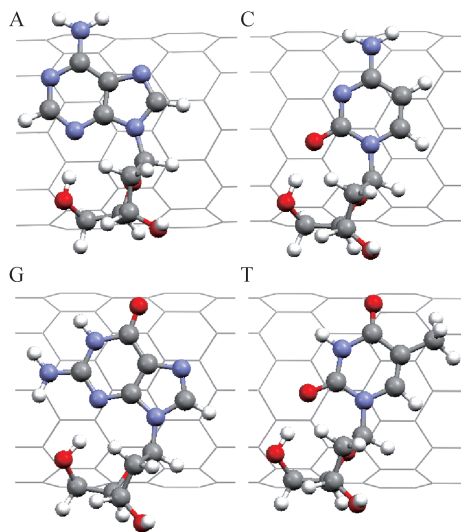

Fig. 7 The most stable configuration for DNA bases (A, C, G, T) adsorption on CNT (10, 0).

In the context of the quantum approach, it is the explicit polarization of electronic charge that contributes to interaction between the nucleosides and the CNT. The local structure, that is, covalent bond lengths and bond angles, shows little deviation from that obtained with the force-field (of order of 0.02 Å and 1°), while the optimal CNT-base distance is reduced by ∼0.3 Å. The base adsorption induces a very small distortion of the CNT geometry, consisting of a 0.02 Å depression on the adsorption side and a 0.007 Å protrusion on the opposite side. The calculated interaction energy is 0.43 to 0.46 eV for the four nucleosides. This value is very close to the LDA calculation of adenine on graphite (0.46 eV) [85] but is significantly lower than the vdW energy of 0.70 to 0.85 eV from the CHARMM calculations (0.70 eV for C, 0.77 eV for T, 0.81 eV for A, and 0.85 eV for G). For comparison, the experimental value extracted from thermal desorption spectroscopy for adenine on graphite is 1.01 eV [86], which is reasonably close to the sum of the dispersion and electronic interaction energies (1.1–1.3 eV). Direct application of vdW-DF to the problem of DNA adsorption on CNT is under way.

4.2 Electronic structure

An essential aspect of the DNA–CNT interaction, and a cornerstone of ultrafast DNA sequencing approaches based on such a combined system, is the electronic structure of its components. The electronic properties of the DNA–CNT can be studied through first-principles quantum mechanical calculations at the single-nucleotide level [11, 87]. The interaction between nucleosides and a CNT is illustrated in Fig. 8(a): in this figure, the density iso-

surfaces of the charge density difference upon adsorption of nucleoside A on the CNT is shown as a representative example of the CNT-nucleoside interaction. The interaction mainly involves the π orbitals of the base atoms, especially the NH_2 group at its end, and of the carbon atoms in the CNT. The sugar group of the nucleoside, on the other hand, shows little perturbation in its electronic cloud, mainly in the region proximate to the CNT.
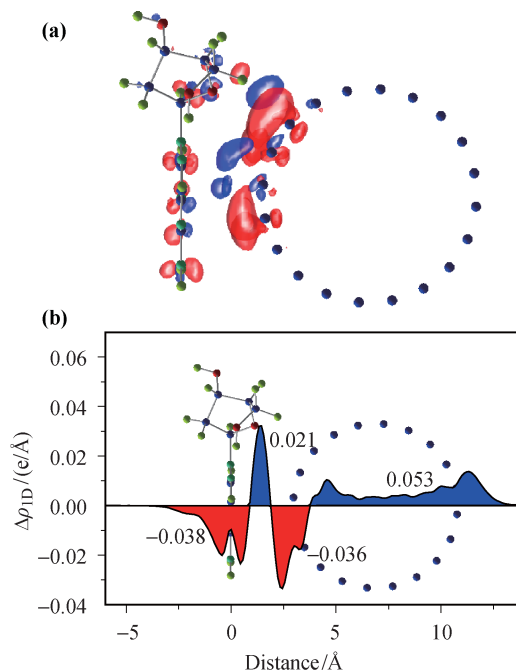

Fig. 8 (a) Isosurfaces of the charge density difference at levels of ± 0.002 e/Å^3 in superposition to the atomic structure for A-nucleoside on CNT. The charge density difference is obtained by subtracting the charge density of the individual A-nucleoside and CNT systems, each fixed at their respective configurations when they are part of the A/CNT complex, from the total charge density of the A/CNT combined system: $\Delta\rho = \rho[A/CNT] - \rho[A] - \rho[CNT]$, where ρ is the charge density. Electron accumulation and depletion regions are shown in blue (+) and red (−), respectively. (b) Planar-averaged charge density along the normal direction to the base plane, illustrating the mutual polarization of π orbitals.

The mutual polarization of π orbitals in the DNA base and the CNT is more obvious in the planar-averaged charge density along the normal to the base plane, as shown in Fig. 8(b). Upon adsorption, the base plane of adenine is positively charged with electron accumulation (near the base) and depletion (near the CNT) in the region between the two components. Integrating this one-dimensional charge distribution in the base and the CNT region, respectively, reveals a net charge transfer of $0.017e$ from A to CNT, assuming the two components are partitioned by the zero difference-density plane close to the CNT wall. This net charge transfer of $0.017e$ from the base to the CNT is rather small compared to that for a typical chemical bond but is consistent with the weak vdW type of interaction between nucleosides and the CNT in this physisorbed system. Moreover, though small it is, this net charge transfer may produce

an enhanced sensitivity in the CNT wall for the detection of molecules attached to it, through measuring, for instance, the shift of Raman peaks in the CNT vibrational modes [88].

A detailed analysis of the contributions to the total energy of the system reveals that the attraction between the nucleoside and the CNT is due to XC interactions. Figure 9 shows the total energy, and the decomposed XC energy and kinetic energy of Kohn–Sham particles as functions of the distance between the DNA base A and the CNT wall. We find that the total energy has a minimum at $d = 3.0$ Å, where the XC energy is negative and the kinetic energy is positive, indicating that the nucleoside-CNT attraction arises from XC effects. Beyond the equilibrium distance, the kinetic energy is lowered and has a minimum at $d = 3.75$ Å, while the XC energy keeps increasing and even becomes repulsive in the range of d=4–5.5 Å. Similar results were found for A adsorbed on graphite [85] and on Cu(110) [89].
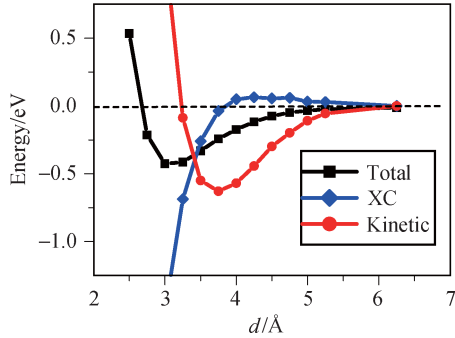
Fig. 9 Relative total energy, the decomposed exchange-correlation (XC) energy and kinetic energy of Kohn–Sham orbits as functions of the base-CNT distance (d) for the DNA base A adsorption on CNT (10, 0).

For a direct real-space identification of DNA bases on CNT, a STM image would be useful. We have simulated the STM images based on the Tersoff–Hamann theory [90]. The STM images in Fig. 10 correspond to the applied voltage of +1.4 V, which integrates the charge densities of states within the energy range of –1.4 to 0 eV below the highest occupied molecular orbital (HOMO, including HOMO). It is clear that the STM images for the four DNA nucleoside have different spacial characteristics, which, with sufficient image resolution, could provide the identification of the four bases directly.
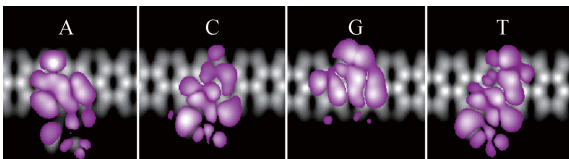

Fig. 10 Simulated STM images of DNA bases on the (10, 0) CNT.

4.3 Optical properties

Hughes *et al.* [91] recently measured the UV-vis absorp-

tion of ssDNA homopolymers consisting of 30 bases wrapped around CNTs in aqueous solution. Different DNA homopolymers show significant differences in optical absorption (both magnitude and peak positions) in the ultraviolet range of 200 to 300 nm. The difference between absorption by the DNA–CNT combined system and the isolated, bare CNT constitutes the absorption signature of the DNA strand attached to the CNT wall. There are significant differences in the obtained spectra from case to case in terms of absorption peak positions and their relative intensity. For instance, there are two peaks for A at 266 and 213 nm, with the second having twice the intensity of the first; there are also two peaks at 275 and 204 nm for C, with the first peak showing higher intensity.

In order to understand the observed DNA absorbance, Meng *et al.* calculated orientation-dependent absorption spectra of DNA bases adsorbed on single-wall CNTs [12], as shown in Fig. 11. The spectra were obtained by aligning the polarization direction of incident light (the direction of the electric field-vector) as those arrows in the insets. All of spectrum changes upon adsorption on CNT can be reproduced accurately. CNTs have a dominant, intrinsic, and diameter-independent absorption peak in the UV region at 236 nm with polarization perpendicular to their axis [92]. Therefore, only photons with polarization parallel to the CNT axis are available to interact with the attached DNA bases, or equivalently, the nanotube produces a local electric field aligned along its axis (the so-called "hypochroism" effect). This explains why the absorption spectra of the DNA bases change when they are attached to the nanotube wall — the direction of tube axis is in fact the preferred direction for UV absorption by the bases. Consequently, the agreement of the calculated changes in absorption with the experimental results strongly suggests that there is a preferred absorption direction for the bases on the CNT, a desirable feature favoring ultrafast DNA sequencing based on optical properties of this system. This result is further supported by the comparison between the calculated linear dichroism curves and the measured ones [93]. Therefore, the arrow in the insets of Fig. 11 also shows the direction of CNT axis, along which the experimental absorbance spectra of ssDNA wrapped on CNTs are best reproduced. The orientations of the nanotube axis relative to the bases as determined from this approach agree well with the global energy-minimum structures from force-field calculations, the only exception being T. Specifically, the directions of the nanotube axis from absorbance spectra, linear dichroism, and structural optimization are 89°, 105°, and 98° for A; –100°, –84°, and –90° for C; –58°, –30°, and –61° for G; and 39°, 40°, and 75° for T. Overall the agreement between experiment and theory is reasonable, given the complicated nature of both the experimental measurements and theoretical
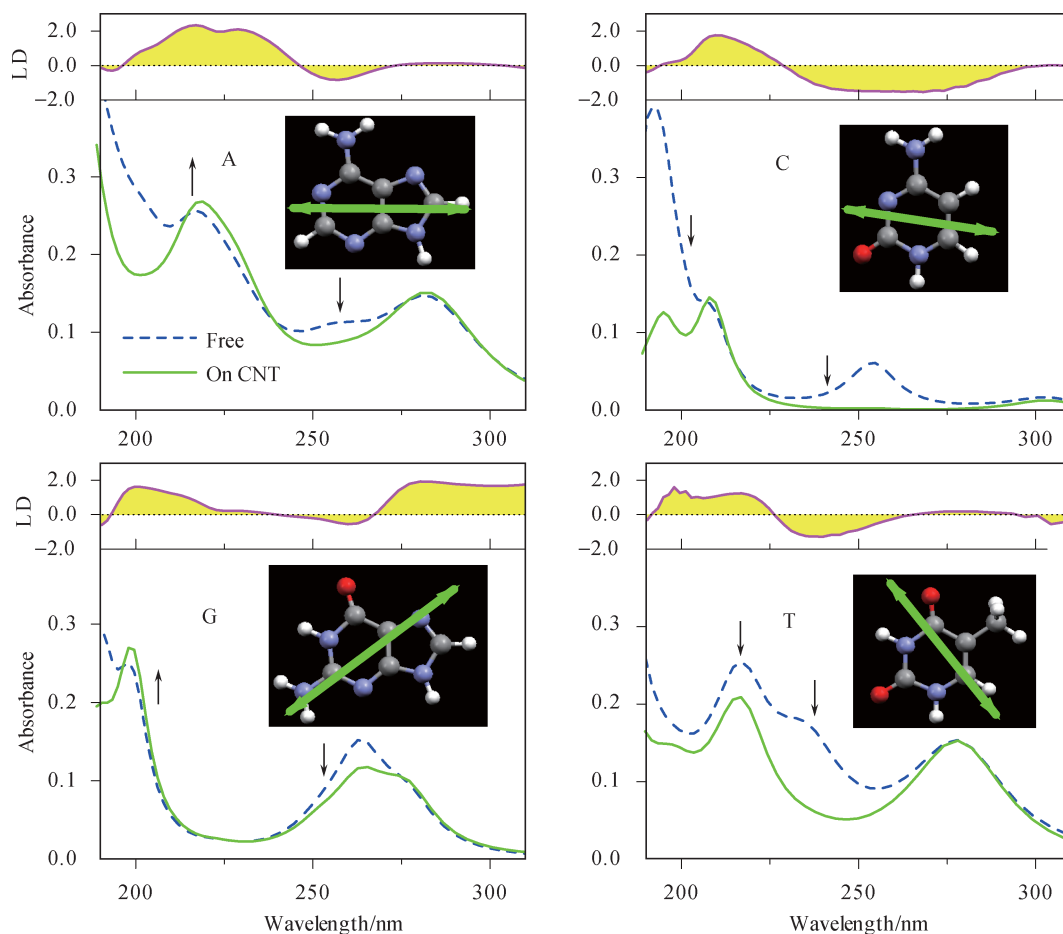
Fig. 11 Absorption spectrum of DNA bases averaged over all field directions (*dashed lines*) and along a particular direction (indicated by double-headed green arrows in the insets) which mimics the nanotube axis (*solid line*). These spectra reproduce adequately the experimentally measured spectra in solution. Vertical arrows indicate intensity changes ("↑" for increase and "↓" for decrease) in experimental spectra after base adsorption on the CNT. Linear dichroism spectra that best match experiment are also shown on top of each panel.

results. This provides a way to determine the base orientation relative to the nanotube axis in the DNA–CNT system from the optical absorption data.

5   Organic dyes binding on oxides

Dye-sensitized solar cells (DSSCs) are believed to be one of the most attractive renewable and low-cost energy solutions, which may replace fossil fuels in the 21st century [1, 13, 14]. A DSSC benefits from its imitation of natural photosynthesis in that it separates sunlight absorption — which requires a large space — from electron collection processes that need highly pure materials and being most efficient on a small length scale. The biggest challenge to develop DSSCs is to realize both functions in the same system and to improve efficiency on both sides.

By combining dye sensitizers with oxide semiconductor nanoparticles, DSSCs resolve this conflict. Visible light absorption efficiency is improved by >1000 times on nanoparticles, compared to that of single-crystal surfaces, due to high surface/volume ratio of

the former [1]. Nevertheless, the stability of the organic dye/semiconductor interface and the mechanism of electron–hole separation upon photoexcitation require careful inspection.

Invoking a quantum mechanical treatment of the dye/TiO_2 interface, Meng *et al.* attacked this problem [13, 14]. They first calculated the binding geometry and energy of representative organic dyes, anthocyanin and model JK dyes, on the stable anatase (101) surface. The most stable binding configuration for cyanidin was determined to be that adsorption onto neighboring Ti ions along [010] via carbonyl and hydroxyl groups of its ring-*B* with Ti–O bond lengths of 1.97 and 1.91 Å, respectively (Fig. 12). Moreover, the calculations reveal that upon adsorption cyanidin transfers the H of the hydroxyl group to the TiO_2 surface, with a small barrier of 0.23 eV. The deprotonation process lowers the system energy by 0.27 eV, resulting in a cyanidin binding energy of 1.0 eV on TiO_2, rendering a stable dye/semiconductor interface at room temperature. More importantly, the deprotonation of cyanidin modifies the electronic structure of the interface: its HOMO is up-shifted into the bandgap
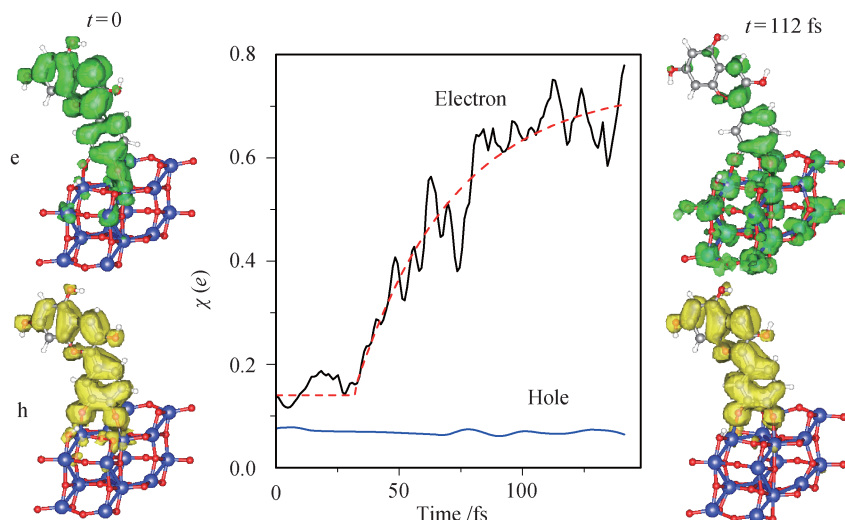
Fig. 12 Electron–hole dynamics after photoexcitation at the organic dye-TiO$_2$ interface. Dashed line is a result fitted by a constant delay followed by an exponential decaying dynamics. Left and right panels show the contour plot at 0.004 e/Å^3 of electron (hole) density upon photoexcitation ($t = 0$) and after separation ($t = 112$ fs).

region of TiO$_2$, and the lowest unoccupied molecular orbital moves toward the edge of conduction band of TiO$_2$. This is critical for electron–hole separation, because excited electrons after sunlight absorption need to inject into the TiO$_2$ conduction band very efficiently.

The electron injection efficiency upon excitation was further investigated using first-principles electron dynamics simulations based on TDDFT [13]. An ultrafast electron-hole separation process at the anthocyanin/TiO$_2$ interface is illustrated in Fig. 12. A pair of electron and hole are generated upon photon absorption at time $t = 0$. Excited electrons will inject into the conduction band of the TiO$_2$ at a time scale of 100 fs, while holes stay stable and confined within the dye molecule. Therefore, they are spacially separated before recombination could take place, contributing to the photocurrent in the solar cell device.

Meng *et al.* also extended to demonstrate further that various factors including dye molecular size, binding geometry, and point defects on the TiO$_2$ surface will influence electron collection efficiency [14]. Experimentally, it is observed that, at various dye/TiO$_2$ interfaces, the timescale of excited electron injection ranges from the shortest 3 fs (biisonicontinic acid, in vacuum) [94] to 100 ps (Ru-complex N719, triplet state injection, in devices) [95]. The huge time span suggests that rich physical factors may play a role. Predicted from exponential decay of tunneling electron density when increasing separation distance in a non-adiabatic process, electron injection will be 3.3 times slower with the addition of a CH$_2$ group inserted between the dye molecule and the semiconductor. This was indeed observed in experiments using Re dyes (ReC1A–ReC3A) [96]. However, this pronounced time increase is not observed in experiments on Zn-porphyrins with one or four oligo(phenylethylny) bridges [97]. From their TDDFT simulations, Meng and

coworkers found that, among the three organic dyes they investigated, longer molecules do involve a longer injection time, which is consistent with intuition. Furthermore, the time elongation is only 1.2 times (by inserting a (CH)$_2$ group) or 1.3 times (inserting a thiophene group). This indicates that adiabatic processes play a major role in these cases, which also explains the Zn-porphyrin experiment [97].

The dye adsorption configurations significantly affect electron injection. By comparing to measured spectra, intact and dissociative dye adsorption are identified. The former is 30 to 50 fs slower than the latter. Different adsorption configurations of intact dyes result in injection time varies by threefold. The difference is mainly caused by the interface dipole moments. A positive dipole at the interface introduces an upshift of conduction band minimum, which will suppress excited electron transfer from the dye molecule to semiconductor conduction bands.

The semiconductor surface also imposes a fundamental influence on electron–hole dynamics. Dye adsorption on surface oxygen vacancies is very stable; it leads to a strong electronic coupling between the dye and the surface resulting in an electron injection time of ∼50 fs, 2 to 3 times faster than that on defect-free surfaces. However, this improvement is at the cost of fast electron–hole recombination, which will reduce device efficiency. These simulations could explain well the two injection times at 40 fs and 200 fs observed in experiments, which would correspond to adsorption on defects and on clean surfaces, respectively.

Besides electron injection, the back transfer of injected electrons was also studied. All these results indicate that electrons and holes are separated in space at a time ∼200 fs, to assure DSSCs work well. Quantum simulations of electron dynamics provide helpful insights and guidelines as to tune the nanoscale and ultrafast processes and to

maximize the energy conversion efficiency of DSSCs.

6   Conclusions

We have applied quantum mechanical simulations based on DFT and TDDFT to address the structure and interaction mechanism of three prototype molecule-surface systems: water/metal, DNA/CNT, and organic dye/TiO$_2$. Based on these studies, some general conclusions can be drawn:

(1) Quantum mechanical calculations yield the binding configuration of molecules on surface as well as the changes in molecular structure upon adsorption, such as dissociation, bond elongation, and bond angle changes. Such a delicate structural information in adsorption systems is not available in empirical simulations, thus representing a unique advantage of quantum simulations. The obtained adsorption structure generally agrees with experimental measurement — the geometry of half-dissociated water layer on Ru(0001) being an exceptional example.

(2) Charge transfer between molecular adsorbate and the substrate is a ubiquitous feature in quantum simulations of molecule–surface interaction. However, the direction and amount of charge transfer vary from case to case depending on the electronic nature of the molecule and the surface. For example, both being a wide-gap but polarizable molecule, water received $0.02e$ from metal surfaces, while DNA bases lose roughly the same amount of electrons to CNTs.

(3) Concerning the dynamics of molecules on surface, both ion dynamics based on DFT forces and electron dynamics based on TDDFT can be carried out in the context of quantum mechanics. Ab initio MD simulations yield an equal-footing treatment of intra- and inter-molecule vibrations, producing accurate, environment-dependent vibrational frequencies, which can be directly compared to experiment and used for molecular recognition. Electron dynamics simulation is more complicated and time-consuming due to its extremely small timestep (∼1 attosecond). Nevertheless, following evolution of electronic wavefunctions, ultrafast electron-hole separation within 200 fs after photoexcitation at the organic dye/TiO$_2$ interface is observed. A systematic investigation of interface electron dynamics identifies a variety of influencing factors and trends. Kinetic parameters, such as diffusion and dissociation energy barrier, can also be obtained from quantum calculations.

(4) New developments in quantum simulations, such as the inclusion of vdW forces into density functionals, quantum nuclei treatments, more accurate exact exchange calculations with random phase approximation [98], and quantum Monte Carlo simulations, improve further the credibility of quantum approaches in describing molecule–surface interactions. The proper inclusion of vdW energies for water adsorption on Cu(110) could possibly lead to a new understanding of water wetting. The quantum nuclear effects in the H-up/H-down water bilayer conversion modifies the classical barriers by tens of meV.

Molecule interaction with important surfaces is essential in many modern technological applications. A quantum approach not only provides accurate atomic structures and energies but also reveals the electronic mechanisms, such as polarization and charge transfer. In addition, dynamics simulations provide direct evidences about stability and reaction pathways and produce spectroscopic data that can be directly compared to experiment as well as to illustrate electron injection and transport at the nanoscale. Thanks to the explosive developments of computer power and improved algorithms during past decades, we have every reason to believe that quantum mechanical simulation will continue to play an even larger role in the course of surface science research.

References

1. M. Grätzel, Acc. Chem. Res., 2009, 42: 1788
2. S. H. Park, A. Roy, S. Beaupre, S. Cho, N. Coates, J. S. Moon, D. Moses, M. Leclerc, K. Lee, and A. J. Heeger, Nat. Photonics, 2009, 3: 297
3. For example, the very popular TIP3P model of water produces an OO distance of 2.75 Å and hydrogen bond angles of −4° and 158° in a water dimer, which are different from the corresponding values in first-principles calculations (2.95 Å, 5°, 125°) and experiment (2.98 Å, −1°, 123°). See S. Meng, Chapter 3, Ph.D. dissertation, Graduatue School of Chinese Academy of Sciences, Beijing, 2004
4. S. Meng, L. F. Xu, E. G. Wang, and S. W. Gao, Phys. Rev. Lett., 2002, 89: 176104
5. S. Meng, E. G. Wang, and S. W. Gao, Phys. Rev. B, 2004, 69: 195404
6. S. Meng, E. G. Wang, C. Frischkorn, M. Wolf, and S. W. Gao, Chem. Phys. Lett., 2005, 402: 384
7. J. Ren and S. Meng, J. Am. Chem. Soc., 2006, 128: 9282
8. J. Ren and S. Meng, Phys. Rev. B, 2008, 77: 054110
9. P. J. Feibelman, Science, 2002, 295: 99
10. J. Carrasco, A. Michaelides, M. Forster, S. Haq, R. Raval, and A. Hodgson, Nat. Mater., 2009, 8: 427
11. S. Meng, P. Maragakis, C. Papaloukas, and E. Kaxiras, Nano Lett., 2007, 7, 45
12. S. Meng, W. L. Wang, P. Maragakis, and E. Kaxiras, Nano Lett., 2007, 7: 2312

13. S. Meng, J. Ren, and E. Kaxiras, Nano Lett., 2008, 8: 3266

14. S. Meng and E. Kaxiras, Nano Lett., 2010, 10: 1238

15. J. M. Soler, E. Artacho, J. D. Gale, A. García, J. Junquera, P. Ordejón, and D. Sánchez-Portal, J. Phys.: Condens. Matter, 2002, 14: 2745

16. P. Hohenberg and W. Kohn, Phys. Rev. B, 1964, 136: 864

17. W. Kohn and L. J. Sham, Phys. Rev. A, 1965, 140: 1133

18. G. Kresse and J. Furthmüller, Phys. Rev. B, 1996, 54: 11169

19. P. E. Blöchl, Phys. Rev. B, 1994, 50: 17953

20. J. P. Perdew, K. Burke, and M. Ernzerhof, Phys. Rev. Lett., 1996, 77: 3865

21. D. R. Hamann, Phys. Rev. B, 1997, 55: 10157

22. S. Kurth, J. P. Perdew, and P. Blaha, Int. J. Quantum Chem., 1999, 75: 889

23. N. Troullier and J. L. Martins, Phys. Rev. B, 1991, 43: 1993

24. D. M. Ceperley and B. J. Alder, Phys. Rev. Lett., 1980, 45: 566

25. M. Dion, H. Rydberg, E. Schröder, D. C. Langreth, and B. I. Lundqvist, Phys. Rev. Lett., 2004, 92: 246401

26. J. Ren, E. Kaxiras, and S. Meng, Mole. Phys., 2010, 108: 1829

27. E. Runge and E. K. U. Gross, Phys. Rev. Lett., 1984, 52: 997

28. S. Meng and E. Kaxiras, J. Chem. Phys., 2008, 129: 054110

29. P. A. Thiel and T. E. Madey, Surf. Sci. Rep., 1987, 7: 211

30. A. Hodgson and S. Haq, Surf. Sci. Rep., 2009, 64: 381

31. G. Held and D. Menzel, Surf. Sci., 1994, 316: 92

32. D. N. Denzler, C. Hess, R. Dudek, S. Wagner, C. Frischkorn, M. Wolf, and G. Ertl, Chem. Phys. Lett., 2003, 376: 618

33. K. Jacobi, K. Bedurftig, Y. Wang, and G. Ertl, Surf. Sci., 2001, 472: 9

34. H. Ogasawara, B. Brena, D. Nordlund, M. Nyberg, A. Pelmenschikov, L. G. M. Pettersson, and A. Nilsson, Phys. Rev. Lett., 2002, 89: 276102

35. S. Meng, L. F. Xu, E. G. Wang, S. W. Gao, Phys. Rev. Lett., 2003, 91: 059602

36. S. Meng, Surf. Sci., 2005, 575: 300

37. A. Glebov, A. P. Graham, A. Menzel, and J. P. Toennies, J. Chem. Phys., 1997, 106: 9382

38. S. Haq, J. Harnett, and A. Hodgson, Surf. Sci., 2002, 505: 171

39. S. Nie, P. J. Feibelman, N. C. Bartelt, and K. Thürmer, Phys. Rev. Lett., 2010, 105: 026102

40. T. Schiros, S. Haq, H. Ogasawara, O. Takahashi, H. Öström, K. Andersson, L. G. M. Pettersson, A. Hodgson, and A. Nilsson, Chem. Phys. Lett., 2006, 429: 415

41. G. Held and D. Menzel, Phys. Rev. Lett., 1995, 74: 4221

42. M. Morgenstern, T. Michely, and G. Comsa, Phys. Rev. Lett., 1996, 77: 703

43. T. Yamada, S. Tamamori, H. Okuyama, and T. Aruga, Phys. Rev. Lett., 2006, 96: 036105

44. J. J. Yang, S. Meng, L. F. Xu, and E. G. Wang, Phys. Rev. Lett., 2004, 92: 146102

45. Y. Yang, S. Meng, and E. G. Wang, Phys. Rev. B, 2006, 74: 245409

46. J. Lee, D. C. Sorescu, K. D. Jordan, and J. T. Yates, J. Phys. Chem. C, 2008, 112: 17672

47. T. Mitsui, M. K. Rose, E. Fomin, D. F. Ogletree, and M. Salmeron, Science, 2002, 297: 1850

48. V. A. Ranea, A. Michaelides, R. Ramírez, P. L. de Andres, J. A. Vergés, and D. A. King, Phys. Rev. Lett., 2004, 92: 136104

49. S. Meng, E. G. Wang, and S. W. Gao, J. Chem. Phys., 2003, 119: 7617

50. K. Morgenstern and J. Nieminen, Phys. Rev. Lett., 2002, 88: 066102

51. A. Michaelides and K. Morgenstern, Nat. Mater., 2007, 6: 597

52. S. Meng, E. Kaxiras, and Z. Y. Zhang, J. Chem. Phys., 2007, 127: 244710

53. M. E. Tuckerman, D. Marx, and M. Parrinello, Nature, 2002, 417: 925

54. J. E. Gunn and B. A. Peterson, Astrophys. J., 1965, 142: 1633

55. D. Marx, M. E. Tuckerman, J. Hütter, and M. Parrinello, Nature, 1999, 397: 601

56. K. Andersson, A. Nikitin, L. G. M. Pettersson, A. Nilsson, and H. Ogasawara, Phys. Rev. Lett., 2004, 93: 196101

57. C. Clay, S. Haq, and A. Hodgson, Chem. Phys. Lett., 2004, 388: 89

58. X. Z. Li, M. I. J. Probert, A. Alavi, and A. Michaelides, Phys. Rev. Lett., 2010, 104: 066102

59. R. S. Smith, C. Huang, E. K. L. Wong, and B. D. Kay, Surf. Sci., 1996, 367: L13

60. P. Löfgren, P. Ahlström, D. V. Chakarov, J. Lausmaa, and B. Kasemo, Surf. Sci., 1996, 367: L19

61. S. Meng, Z. Zhang, and E. Kaxiras, Phys. Rev. Lett., 2006, 97: 036107

62. M. Zheng, A. Jagota, E. D. Semke, B. A. Diner, R. S. Mclean, S. R. Lustig, R. E. Richardson, and N. G. Tassi, Nat. Mater., 2003, 2: 338

63. M. Zheng, A. Jagota, M. S. Strano, A. P. Santos, P. Barone, S. G. Chou, B. A. Diner, M. S. Dresselhaus, R. S. Mclean, G. B. Onoa, G. G. Samsonidze, E. D. Semke, M. Usrey, and D. J. Walls, Science, 2003, 302: 1545

64. B. Gigliotti, B. Sakizzie, D. S. Bethune, R. M. Shelby, and J. N. Cha, Nano Lett., 2006, 6: 159

65. D. A. Heller, E. S. Jeng, T. K. Yeung, B. M. Martinez, A. E. Moll, J. B. Gastala, and M. S. Strano, Science, 2006, 311: 508

66. Y. Xu, P. E. Pehrsson, L. Chen, R. Zhang, and W. Zhao, J. Phys. Chem. C, 2007, 111: 8638

67. G. O. Gladchenko, M. V. Karachevtsev, V. S. Leontiev, V. A. Valeev, A. Y. Glamazda, A. M. Plokhotnichenko, and S. G. Stepanian, Mole. Phys., 2006, 104: 3193

68. H. J. Gao, Y. Kong, D. Cui, and C. S. Ozkan, Nano Lett., 2003, 3: 471

69. H. J. Gao and Y. Kong, Annu. Rev. Mater. Res., 2004, 34: 123

70. T. Okada, T. Kaneko, R. Hatakeyama, and K. Tohji, Chem. Phys. Lett., 2006, 417: 288

71. J. D. Watson and F. H. C. Crick, Nature, 1953, 171: 737

72. S. Iijima, Nature, 1991, 354: 56

73. J. Li, H. T. Ng, A. Cassell, W. Fan, H. Chen, Q. Ye, J.

Koehne, J. Han, and M. Meyyappan, Nano Lett., 2003, 3: 597

74. N. W. S. Kam, Z. A. Liu, and H. J. Dai, Angew. Chem. Int. Ed., 2006, 45: 577

75. C. Staii, A. T. Johnson, M. Chen, and A. Gelperin, Nano Lett., 2005, 5: 1774

76. G. Lu, P. Maragakis, and E. Kaxiras, Nano Lett., 2005, 5: 897

77. A. Star, E. Tu, J. Niemann, J. P. Gabriel, C. S. Joiner, and C. Valcke, Proc. Natl. Acad. Sci. USA, 2006, 103: 921

78. E. S. Jeng, A. E. Moll, A. C. Roy, J. B. Gastala, and M. S. Strano, Nano Lett., 2006, 6: 371

79. B. R. Brooks, R. E. Bruccoleri, B. D. Olafson, D. J. States, S. Swaminathan, and M. Karplus, J. Comp. Chem., 1983, 4: 187

80. A. D. MacKerell, D. Bashford, M. Bellott, R. L. Dunbrack, J. D. Evanseck, M. J. Field, S. Fischer, J. Gao, H. Guo, S. Ha, D. Joseph-McCarthy, L. Kuchnir, K. Kuczera, F. T. K. Lau, C. Mattos, S. Michnick, T. Ngo, D. T. Nguyen, B. Prodhom, W. E. Reiher, B. Roux, M. Schlenkrich, J. C. Smith, R. Stote, J. Straub, M. Watanabe, J. Wiórkiewicz-Kuczera, D. Yin, and M. Karplus, J. Phys. Chem. B, 1998, 102: 3586

81. S. V. Krivov, S. F. Chekmarev, and M. Karplus, Phys. Rev. Lett., 2002, 88: 038101

82. R. Elber and M. Karplus, Science, 1987, 235: 318

83. D. J. Wales and H. A. Scheraga, Science, 1999, 285: 1368

84. D. J. Wales, Science, 2001, 293: 2067

85. F. Ortmann, W. G. Schmidt, and F. Bechstedt, Phys. Rev.

Lett., 2005, 95: 186101

86. J. E. Freund, Ph.D. thesis, Ludwig–Mmaximilians Universität München, 1998

87. A. N. Enyashin, S. Gemming, and G. Seifert, Nanotechnology, 2007, 18: 245702

88. C. Fantini, A. Jorio, A. P. Santos, V. S. T. Peressinotto, and M. A. Pimenta, Chem. Phys. Lett., 2007, 439: 138

89. M. Preuss, W. G. Schmidt, and F. Bechstedt, Phys. Rev. Lett., 2005, 94: 236102

90. J. Tersoff and D. R. Hamann, Phys. Rev. B, 1985, 31: 805

91. M. E. Hughes, E. Brandin, and J. A. Golovchenko, Nano Lett., 2007, 7: 1191

92. Y. Murakami, E. Einarsson, T. Edamura, and S. Maruyama, Phys. Rev. Lett., 2005, 94: 087402

93. J. Rajendra and A. Rodger, Chem. Eur. J., 2005, 11: 4841

94. J. Schnadt, P. A. Bruhwiler, L. Patthey, J. N. O'Shea, S. Sodergren, M. Odelius, R. Ahuja, O. Karis, M. Bassler, P. Persson, H. Siegbahn, S. Lunell, and N. Martensson, Nature, 2002, 418: 620

95. S. A. Haque, E. Palomares, B. M. Cho, A. N. M. Green, N. Hirata, D. R. Klug, and J. R. Durrant, J. Am. Chem. Soc., 2005, 127: 3456

96. J. B. Asbury, E. Hao, Y. Wang, and T. Lian, J. Phys. Chem. B, 2000, 104: 11957

97. C. W. Chang, L. Luo, C. K. Chou, C. F. Lo, C. Y. Lin, C. S. Hung, Y. P. Lee, and E. W. Diau, J. Phys. Chem. C, 2009, 113: 11524

98. L. Schimka, J. Harl, A. Stroppa, A. Grüneis, M. Marsman, F. Mittendorfer, and G. Kresse, Nat. Mater., 2010, 9: 741